Solvothermal Synthesis of Sm^{3+}-doped Fe_3O_4 nanoparticles

T.A. Lastovina,[a*] A.P. Budnyk,[a] E.A. Kudryavtsev,[b] A.V. Nikolsky,[c] A.T. Kozakov,[c] N.K. Chumakov,[d] A.V. Emelyanov,[d] and A.V. Soldatov [a]

[a] International Research Center "Smart materials", Southern Federal University, 5, Zorge Str., Rostov-on-Don, 344090, Russia

[b] Joint Research Center "Diagnostics of structure and properties of nanomaterials", Belgorod National Research University, 85, Pobedy Str., Belgorod, 308015, Russia

[c] Research Institute of Physics, Southern Federal University, 194, Stachkiave., 344090, Russia

[d] National Research Centre "Kurchatov Institute", 1, Akademika Kurchatova sq., Moscow, 123182, Russia

***Corresponding author:** T.A. Lastovina, e-mail: lastovina@sfedu.ru

Abstract:

Magnetic iron oxide nanoparticles doped with samarium were prepared by solvothermal polyol method. An introduction of 2,2'-bipyridine during the synthesis reduces the particle diameter to about 9 nm in average. The difference in physical and magnetic properties of the samples prepared with and without capping agent was outlined on the basis of complex characterization by a number of experimental techniques. The characteristics of resulted product make it suitable for biomedical applications, for instance, as a contrast agent for MRI.

Highlights:

- Sm^{3+}-doped magnetite nanoparticles were obtained by solvothermal polyol method,
- Magnetic nanoparticles are twice smaller if 2,2'-bipyridine is used as a capping agent,
- Sm^{3+}-doped magnetite nanoparticles have clean surface and are useful as a MRI contrast agent.

Keywords: Nanoparticles; Magnetite; Solvothermal synthesis; Rare-earth doping; Bipyridine

1. Introduction

An indubitable importance of novel, property-modified nano-sized magnetic materials for numerous demanding applications in biomedicine, electronics and catalysis has been fueling scientific research from the beginning of a nanotechnology era [1]. Among the mentioned fields biomedicine alone employs magnetic nanoparticles (MNPs) in many different ways, to mention a few as carriers for genetic materials [2], as hybrid nano-vehicles for remotely controlled therapeutic delivery [3], as vessels for drugs and contrast agents for magnetic resonance imaging (MRI) [4], as heat mediators for cancer hyperthermia treatment and labels for separation and purification of molecules in bioprocesses [5] and activators in neuronal modulation [6]. The next generation of MRI contrast agents is expected to sophistically exploit such firmly features of MNPs as enhanced magnetic moments due to high payload of Fe or other "magnetic" metals [7]. Prominent examples from the emerging field include iron oxides doped with rare earth elements [8], multi-purpose magnetic anisotropic Janus particles [9], nanoparticles incorporated into polymeric hydrogels [10]. Among them the superparamagnetic iron oxide nanoparticles (SPIONs) are produced by several routes including the hydrothermal technique, chemical co-precipitation, microwave irradiation, thermal decomposition etc [11, 12]. Since the physical properties of MNPs are strongly related to their morphology and dimension, all the synthesis methods are heading towards control over the crystallite size, shape, extent of agglomeration and their surface chemistry. And in the most cases due to inevitable drawbacks of any given method there is a need to add some surfactant for better control over particle growth, and then to stabilize MNPs by using both electrostatic and steric repulsive forces [13]. Hence, it is still a challenge to prepare MNPs of suitable and uniform size.

Motivated by a call for a simple method allowing a reproducible formation of small (~10 nm) magnetite (Fe_3O_4) MNPs, we have developed a novel synthesis protocol based on a solvothermal method. This method is already known to produce uniform MNPs down to 5 nm in diameter having potential for MRI application [14]. For instance, Ooi *et al.* [15] reports a solvothermal synthesis of Fe_3O_4 octahedrons with ~90 nm edge from $FeCl_3$ in ethylene glycol (EG). These anisotropic nanostructures have been obtained by studying the influence of 1,3-diaminopropane on EG/oleylamine-based solutions. Keeping EG as a traditional reliable solvent for a reaction medium, we decided to involve a new stabilization agent from the bipyridine isomers line, namely, 2,2'-bipyridine (Bpy). Being an uncommon participant to the synthesis protocols for MNPs, bipyridines as N-donor compounds have been already employed for protection of transition metal clusters against their agglomeration in solution [16].

Transition metals (Co, Ni, Mn and Pt) are known to be effective dopants of MNPs with the scope to improve their magnetic properties [17]. Compared to them, lanthanides (Ln) have much stronger potential in expressing pronounced magnetic features due to large unquenched orbital angular momentum attributed to the *f* electrons demonstrating higher spin-orbit coupling. This is why the substitution of Fe^{3+} in magnetite with rare earth ions like Sm^{3+} or Eu^{3+} could improve magnetic and optical properties of $Ln:Fe_3O_4$ materials [18]. Co-precipitation in an alkaline solution and a reverse micelle method both reportedly are lacking a good control over the particle size distribution, while thermal decomposition of a mixture containing $Fe(acac)_3$ and $Ln(acac)_3 \cdot 2H_2O$ (acac = acetylacetonate) in the presence of passivating surfactants allows to obtain the diamond-shaped $Sm:Fe_3O_4$ particles with an average size of 12 nm [19].

In this work, we report the study on structural and magnetic properties of Sm^{3+}-doped iron oxide MNPs grown by solvothermal polyol method from a mixture of metal chlorides with particular focus on the changes in MNPs modulated by introduction of 2,2'-bipyridine into the reaction solution.

2. Material and methods

2.1. Chemicals

Iron(III) chloride ($FeCl_3$, 97%) was obtained from Sigma-Aldrich. Ethylene glycol (EG, C_2H_6O, 99%), 2,2'-bipyridine ($C_{10}H_8N_2$, 99+%), sodium hydroxide (NaOH, 98%), ultra dry samarium chloride ($SmCl_3$, 99.9%, REO) were supplied by Alfa Aesar. All chemicals were of analytical grade standards and used as received. Deionized (DI) water (18 MΩ·cm at 25 °C) was obtained by using SimplicityUV ultra-pure water system.

2.2. Synthesis of magnetic NPs

The two sets of Sm^{3+}-doped iron oxide NPs were produced by a solvothermal method without and with addition of a capping agent. In the first case, $FeCl_3$ ($4\cdot10^{-3}$mol) and $SmCl_3$ ($1.35\cdot10^{-4}$ mol) were dissolved in 40 mL of EG. Then, NaOH ($2.4\cdot10^{-2}$ mol) in EG solution (10 mL) was added to reach pH≈10. The solution has been purging with argon for 10 min to reduce oxygen content. Then the solution was poured in a Teflon-lined stainless-steel high pressure reactor (Berghof BR-200), where it has been maintained at 200 °C for 72 h under magnetic stirring. The reactor was cooled down to room temperature (RT). A black precipitate was washed several times with ethanol and DI water and retrieved by magnetic decantation. The powder was dried in a vacuum oven at 60 °C overnight. Another sample was prepared following the same procedure, with the only difference that 2,2'-bipyridine ($4\cdot10^{-3}$ mol) in 10 mL EG was added to the starting mixture of $FeCl_3$, $SmCl_3$ and NaOH in EG. The magnetic NPs prepared without a stabilization agent will be further referred as Sm:MNPs, and those obtained with addition of 2,2'-bipyridine as Sm:MNPs-Bpy.

2.2. Instrumentation

X-ray diffraction (XRD) patterns were collected with Ultima IV powder diffractometer (Rigaku) using CuKα radiation (α = 1.5406 Å) with a 0.02° step size and a 2 s dwell time. Operating conditions were 40 kV and 40 mA. The XRD patterns were processed by Rigaku PDXL Software: profile fitting for phase identification was performed using the WPPF (Whole Powder Pattern Fitting) method and crystallite size was calculated by Scherrer and Williamson-Hall methods [20]. For the former method the values of crystallite size obtained for each reflex in 25 to 80° 2θ interval were averaged.

TEM images were acquired using JEM-2100 microscope (JEOL) operated at an accelerating voltage of 200 kV. The samples were prepared by dropping a dilute dispersion of the sample in isopropanol onto a copper mesh coated with a carbon layer and then allowing the solution to dry at RT. The particle size distribution was obtained by direct measurements of individual particles in the complete set of TEM images, constituting a set of about 100 particles.

Thermogravimetry analysis (TGA) of samples was performed using a SDT Q600TGA/DSC analyzer (TA Instruments), allowing for simultaneous recording of weight change and differential scanning calorimetry (DSC) curves on the same sample. Samples of about 22 mg weight in alumina crucibles were heated from room temperature to 800 °C at 10 $°C \cdot min^{-1}$ rate under argon flow.

Ultra Violet – Visible (UV-Vis) spectra were recorded on UV-2600 spectrophotometer (Shimadzu) with 2 nm resolution. In transmittance mode solutions of the sample against EG were measured in 2 mm cuvettes. Diffuse-reflectance (DR) spectra were recorded with integrating sphere accessory. Samples were mixed with barium sulfate and pressed into discs to be measured against pure $BaSO_4$. The obtained reflectance values (%R) were converted into Kubelka-Munk function values using the instrument's software.

The Fourier transform infrared (FTIR) spectra were collected in the air using Bruker Vertex 70 spectrometer (at 64 scans with resolution of 2 cm^{-1}) employing the KBr pellet technique.

Micro X-ray Fluorescence (XRF) analysis was done using Bruker M4 TORNADO Micro-XRF spectrometer. The sample powder was deposited on the surface of boric acid disk. The resulted data were averaged over several measured points and presented in both atomic % (at %) and weight % (wt %).

X-ray photoelectron spectra (XPS) were obtained using ESCALAB 250 spectrometer with excitation by monochromatized Al Kα-line radiation (hν = 1486.6 eV). A thin layer of finely powdered sample was deposed on a conductive carbon tape and fixed in a standard stainless steel sample holder. The size of an X-ray focal spot on the sample's surface was 350 x 500 microns. The elemental composition of the sample was determined by the spectra taken at an analyzer pass energy of 150 eV, while the C1s, O1s, Fe2p core lines were recorded with the pass energy of 20 eV. The spectrometer was calibrated in advance using the Ag $3d_{5/2}$ (368.2 eV) and Au $4f_{7/2}$ (84.0 eV) bonding energies lines derived from the reference metal surfaces cleaned with a flow of argon ions. The minimal energy range allowed in the experiment was measured on the full width at half maximum (FWHM) of the Ag $3d_{5/2}$ line being not worse than 0.6 eV. To remove a weak positive charge from the sample's surface it was irradiated by 2 eV "slow" electrons. XPS spectra were referenced to the C1s carbon line at binding energy of 285.0 eV. The XPS spectra were processed using Avantage software. The background subtraction was done using the Shirley method and spectral deconvolution into mixed 30% Lorentzian + 70% Gaussian symmetrical components was performed.

Magnetic curves M (H) were measured using a vibrating sample magnetometer (VSM) 7400 (Lake Shore Cryotronics). Experiments were carried out in magnetic field up to 10 kOe at RT (295 K). The sample powder was tightly pressed into the space between two parts of polymer capsules with spherical bottom size about Ø 4.5 mm. The polymer capsule contribution to magnetic signal was negligible. The magnetization error due to the sample shape was below 5%, which has been controlled by rotation of the sample. The mass measurement error was less than 1%.

3. Experimental results

The XRD patterns for both samples are presented in Fig. 1 together with ICDD crystallographic database reference [21a] for magnetite. The observed reflexes at 2θ about 30, 35, 37, 43, 53, 57, 62 and 74° can be indexed into a cubic spinel structure of Fd-3m space group. Profile analysis has concluded a good match of samples crystallinity with ICDD crystallographic database records ([21b] for Sm:MNPs-Bpy and [21c] for Sm:MNPs) related to spinel. The values obtained for lattice parameter α are given in Table 1, both of them being slightly higher than value of $\alpha = 8.387$ Å known for Fe_3O_4 magnetite [21-14a]. The increased α value in our samples can be explained by the substitution of Fe^{3+} ions with the larger Sm^{3+} ions (having radii of 0.64 and 0.96 Å, respectively) [22], which causes an internal stress and expansion of the cell unit. More precisely, Sm^{3+} ions have a strong tendency to enter B-sites in the spinel lattice [23]. These octahedral interstitial sites could accommodate a few percents of larger guest ions without significant lattice distortion, but at higher loadings (i.e. 3%, [18]) Sm^{3+} ions may also occupy smaller tetrahedral A-sites resulting in appreciable lattice expansion.

From Fig. 1 it comes clear that reflexes from Sm:MNPs-Bpy sample are about double broader and twice less intense than those from Sm:MNPs sample, although, expressing similar profiles of their relative intensities. Respectively, the average crystallite size was evaluated to be 7-9 nm for Sm:MNPs-Bpy and 25 nm for Sm:MNPs (see Table 1). No appreciable reflexes due to other crystalline phase were observed in XRD patterns. This allows to assume that doped Sm^{3+} ions are highly dispersed in the spinel phase without any evident distortion of crystallinity, what has been already observed for Ln:Fe_3O_4 systems [18, 19].

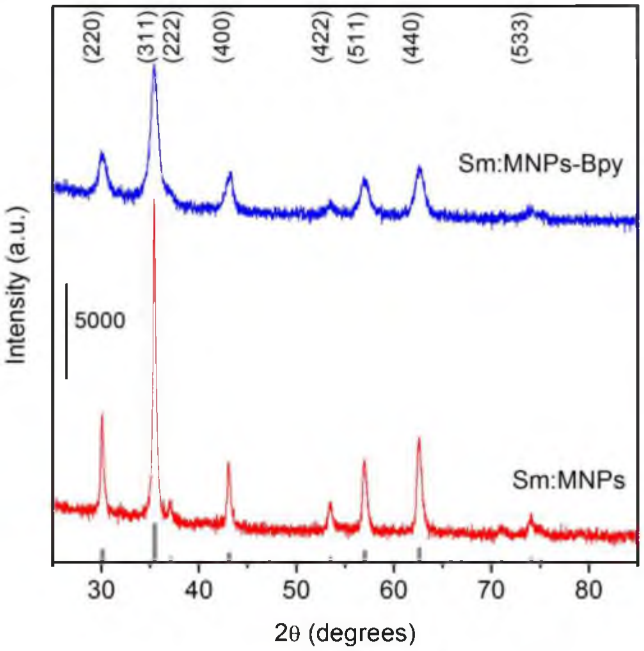

Fig.1. XRD patterns of Sm:MNPs (red) and Sm:MNPs-Bpy (blue) samples prepared solvothermally. Gray bars in bottom show theoretical reflexes for Fe_3O_4 magnetite phase.

Table 1. XRD and TEM analysis data for Sm:MNPs and Sm:MNPs-Bpy samples.

Sample name	Phase name	Space group	Lattice parameter, *a* (Å)	Crystallite size, *d′* (nm)	Crystallite size, *d″* (nm)	Particle size, *d** (nm)
Sm:MNPs	Magnetite, syn	Fd-3m	8.3972	24.5 ± 2.30	24.7607	23.8
Sm:MNPs-Bpy	Magnetite	Fd-3m	8.3936	8.9 ± 0.83	6.9134	9.6

Note: crystallite size *d′* is calculated by Sherrer's relation, and *d″* – by Williamson-Hall method. Particle size *d** obtained from the analysis of TEM images.

The representative TEM images for both Sm:MNPs and Sm:MNPs-Bpy samples are shown in Fig. 2 together with histograms of particle size distribution. The histograms show normal distribution profiles and the number-based mean particle size over 100 counted particles of the Sm:MNPs sample is ~ 23.8 nm and that of the MNPs-Bpy sample is 9.6 nm (Table 1). As it can be seen from Fig. 2 both samples are composed of agglomerated (to different extent) particles exhibiting round-like polyhedral shapes, but some of them can be easily attributed to octahedrons. An octahedral morphology is thermodynamically favored over other possible geometries due to exposure of the lowest energy crystal facets to the environment [24]. Spherical particles are formed when isotropic surface coverage of the growing nuclei occurs by more homogeneous solvent/surfactant environment [15]. The average particle size values obtained from TEM results are in a good agreement with those calculated from XRD data (see Table 1).

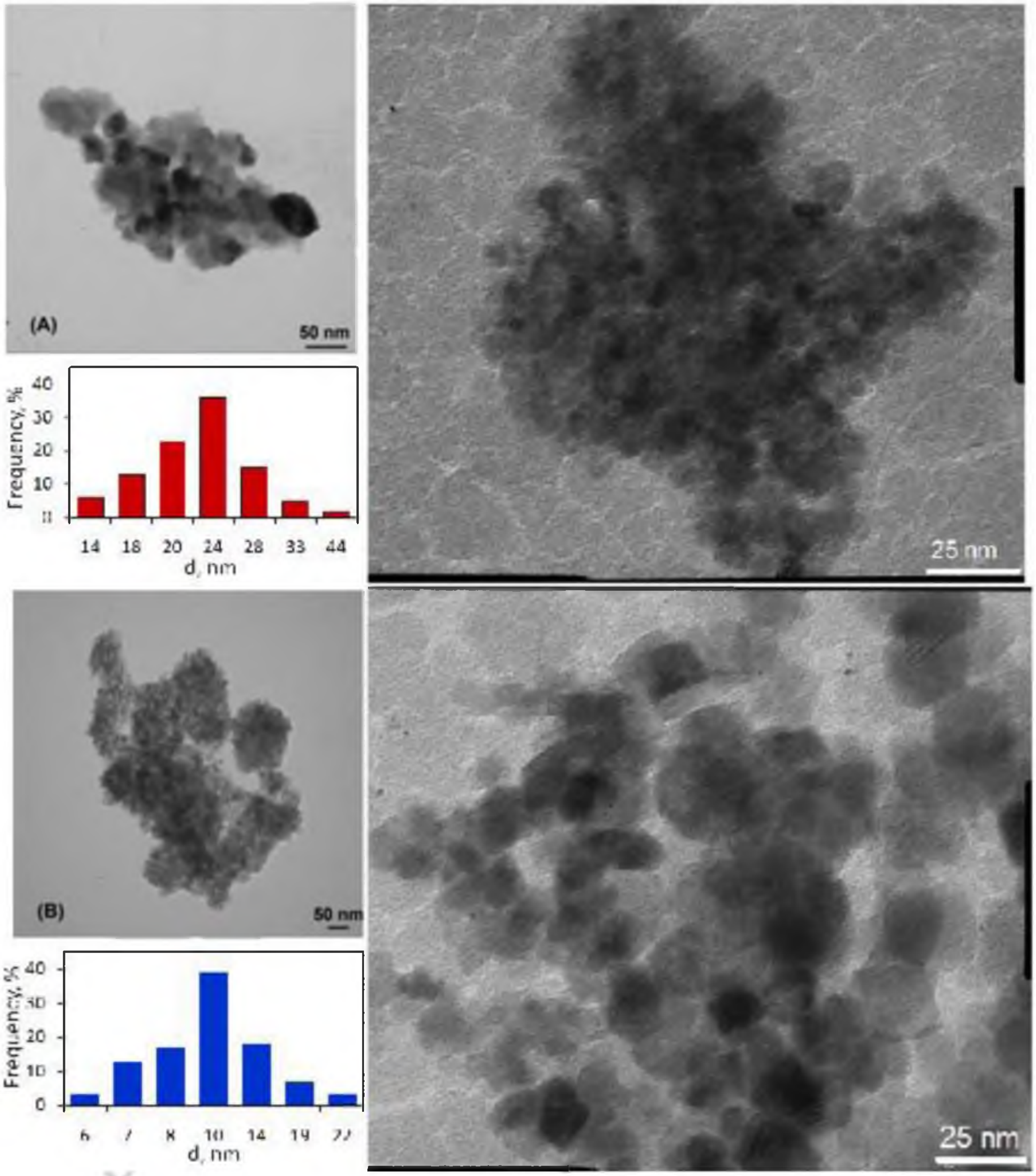

Fig. 2. TEM images of MNPs (A) and MNPs-Bpy (B) samples with respective particle size distributions.

TGA weight loss curves along with derivatives are presented in Fig.3a. This type of profile has been already observed for magnetite NPs prepared in polyol medium [25]. The route of curves can be roughly divided into three intervals: 25-200, 200-500 and 500-800 °C. The initial weight loss (~ 3 %) is clearly caused by removal of surface adsorbed water occurring in both samples at 50-100 °C. After that in the same interval the Sm:MNPs sample continues to lose the weight (at ~ 150 °C), while its counterpart does not. This phenomenon can be attributed to removal of residual free EG, which seemingly is more abundantly present in the MNPs sample. In the next interval both samples are experienced a noticeable weight loss (Sm:MNPs of 6.4% and Sm:MNPs-Bpy of 9.2% totally at 500 °C), with derivative curves showing three distinct peaks at about 230, 285 and 370 °C. This weight decrease is attributed to the desorption of EG covering the surface of MNPs. The difference in integral area under these three peaks of derivative curves is about two. This values is in accordance with what one might expect taking into account the difference in average size of particles in both samples. In the highest temperature interval the Sm:MNPs-Bpy only shows appreciable (6.4 %) weight loss, which might be attributed to the destructive coalescence of small particles with possible change of Fe oxidation state. Heat capacity curves (Fig. 3b) exhibit similar profile with the most visible difference at the beginning of a measurement.

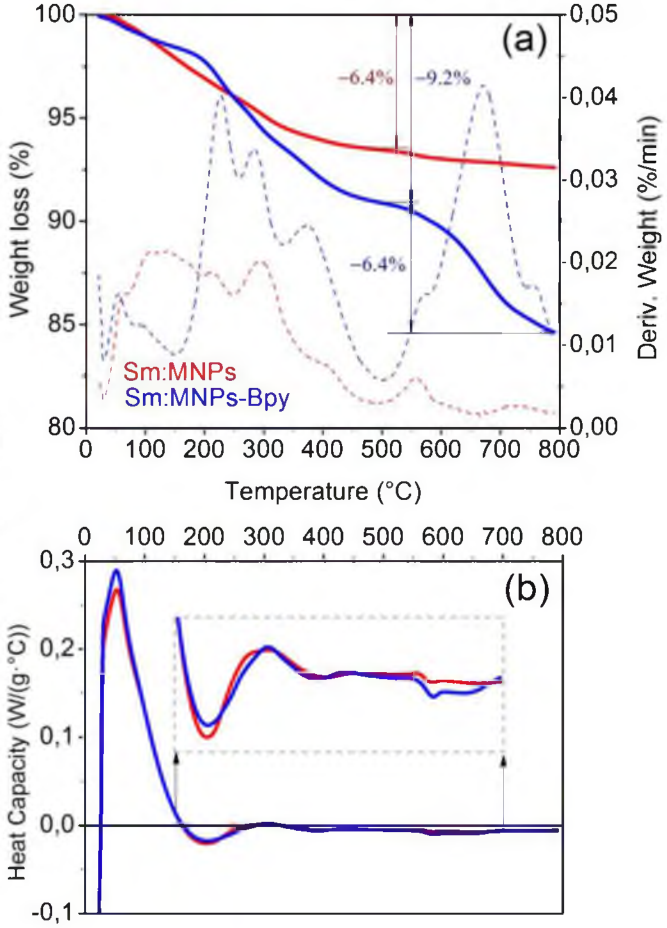

Fig. 3.TGA (a) and DSC (b) curves of Sm:MNPs (red) and Sm:MNPs-Bpy (blue) samples, shown together with derivative of weight loss (a).

The mixture of metal chlorides has a brown-yellowish color. Its optical spectrum is presented in Fig. 4a (red curve). Upon addition of 2,2'-Bpy the color of solution does not change at RT, but turning to wine-red when temperature reaches ~ 100 °C (Fig. 4a blue curve). Solution also darkened, and in order to better appreciate the profile of newly formed absorbance band at ~ 500 nm (with two peaks at 490 and 522 nm) a diluted with EG 1:5 vol. solution was recorded too (dashed blue curve in Fig. 4a). Such color changes have been already observed for iron-bipyridyl complexes, absorbing at 530 nm [26]. Further considerations about possible chemistry of the synthesis process will be provided below.

The DRUV-Vis spectra for the obtained MNPs are shown in Fig. 4b. They have a similar profile, and the difference in intensity primary relates to some variations in sample coverage under the beam light. The spectral curves show a strong absorbance in UV region, which is steady decreasing until 600 nm and then continues with another band rising towards higher wavelengths. Such reflectivity profile is count to be typical for magnetite, whose interband transitions had been already described [27]. Sm:MNPs sample exhibit somehow degraded reflective profile in comparison with Sm:MNPs-Bpy, which might be indicative for the presence of other oxide impurities, like maghemite [28].

FTIR spectra are shown in Fig. 4c. They exhibit a similar sequence of bands for both samples, the fact pointing on their equivalence in chemical composition. The dominating couple of bands at 582 and 400 cm^{-1} are due to Fe–O bonds of MNPs. The rest of bands relates to the species adsorbed on MNPs surface. In particular, a broad band peaking at 3400 cm^{-1} is formed by OH stretching mode coming from the surface hydroxyls and adsorbed water (inevitable in the adopted technique). Respective bending mode is situated at 1640 cm^{-1}. Stretching modes of methylene groups are visible at 2928 ($\nu_{as}CH_2$) and 2856 (ν_sCH_2). The groups of bands centered around 1500 and 1100 cm^{-1} are the envelopes, containing bending modes of hydrocarbons and carboxylate stretching modes. As an example the deconvolution of first envelope is shown as inset in Fig. 4c. The first envelope contains common vibrations for both samples falling at 1640 cm^{-1} (δOH), 1586 and 1380 cm^{-1} (ν_{as}CO and ν_sCO, respectively) and 1380 cm^{-1} (δCH). to MNPs surface that The second envelope at 1100 cm^{-1} contains three components situated atabout 1120, 1080 and 1040 cm^{-1}, with the first attributed to C–O–C, while later two formed by CO vibrations. Presence of these moieties is clearly ascribed to residual hydroxyls and EG molecules covering the surface of MNPs and was observed in similar cases [25]. The large difference $\Delta = \nu_{as}CO - \nu_sCO = 206$ cm^{-1} suggests a unidentate coordination of EG ligands to MNPs surface via carboxylate group [29-22]. More detailed analysis of IR bands lays out of the scope of this work.

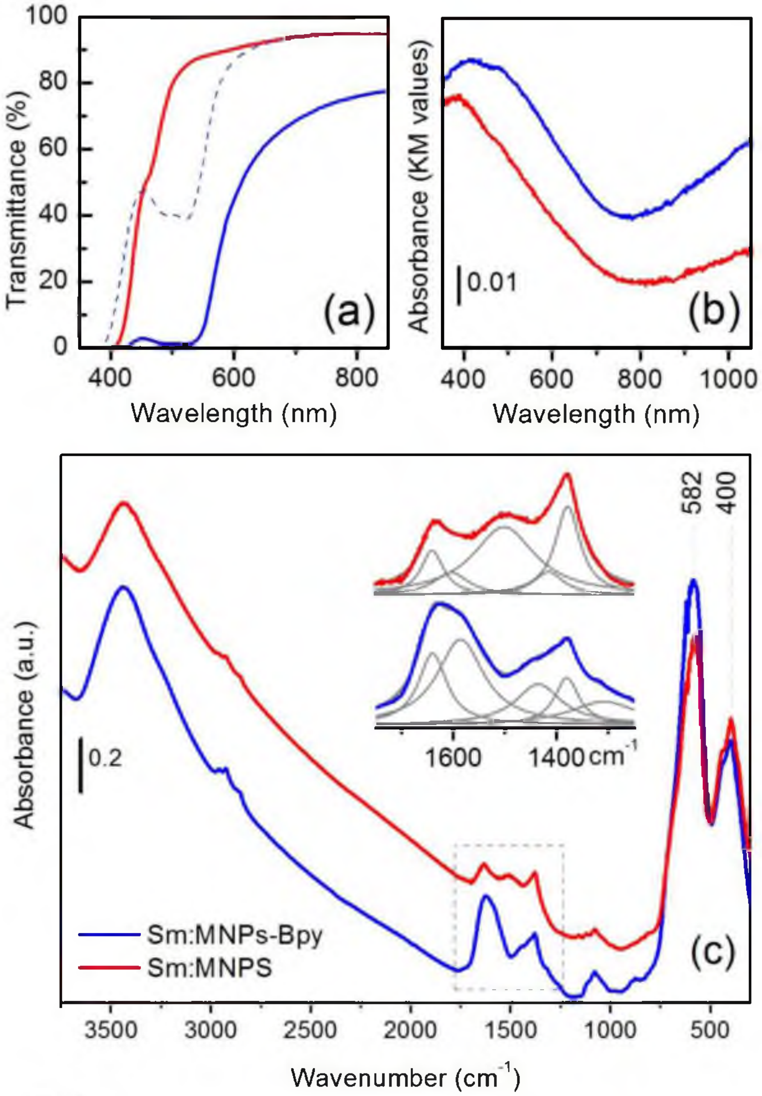

Fig.4. UV-Vis (a, b) and FTIR (c) spectra of Sm:MNPs (red) and Sm:MNPs-Bpy (blue) samples: (a) UV-Vis spectra of reaction mixtures at 100 °C in transmittance, (b) UV-Vis of resulting MNPs in reflectance, (c) FTIR of resulting MNPs in KBr pellets with a zoomed interval presenting deconvolution of complex spectral profile.

After morphology and surface properties of MNPs having been described the key question to address experimentally is their elemental composition, with particular focus on samarium quantity. For this purpose, we employed two X-ray based techniques: XPS and XRF (the results are summarized in Table 2). In particular, XRF measurements over several spots of each samples revealed that Sm content in relation to Fe makes about 7.3 wt% (2.8 at%) in Sm:MNPs-Bpy sample, and 5.9 wt% (2.3 at%) in Sm:MNPs one. Being compared with loading value of 8.3 wt% (3.3 at%), which was the same for both samples, one can find that more samarium were remained when 2,2'-Bpy had been used: 87 % (Sm:MNPs-Bpy) against 70 % (Sm:MNPs). It should be also mentioned here, that adopted synthesis protocol preserves more samarium in the sample in comparison to other solvothermal polyol routes reported in the literature. For example, in ref. [18] about 61 wt% of Sm was remaining in average as evaluated by EDS (Energy-dispersive X-ray spectroscopy) analysis.

The further inquiry into elemental composition was performed by using XPS measurements (Table 2). It is known, that for solid samples, single crystals and ceramics having surfaces processed in ultrahigh vacuum by scribing or cutting the energy position of Fe2p$_{3/2}$ peak of iron(III) lies in the range of 711.0-711.2 eV [23], that of iron(II) at 710.3 eV [33], and in Fe_3O_4 magnetite in the range of 710.6 -711.4 [32-25]. Fe2p spectra for both samples are shown in Fig. 5. Each Fe2p spectrum consists of two main peaks A and C, corresponding to 2p$_{3/2}$ and 2p$_{1/2}$ of Fe, arising from the spin-doublet splitting of 2p level. At the low-energy tail of Fe2p$_{3/2}$ peak there is a poorly developed shoulder A' located approximately at 2.7-3 eV below the main peak. In our case of powdered samples, the energy position of Fe2p$_{3/2}$ peak in Sm:MNPs-Bpy falls at 710.9 eV, and that of Sm:MNPs stays at 710.5 eV.

However, the energy position of Fe2p$_{3/2}$ peak cannot be the only criteria for determination the oxidation state of iron ions in the powdered samples, prepared under air atmosphere. As shown in Table 2, except iron and samarium lines there are also lines of carbon and oxygen present on the surface of MNPs. Deconvolution of C1s and O1s spectra into the components and their analysis shows that in addition to the main peak with E_b = 285.0 eV (almost 70% of total content) corresponding to hydrocarbons, there are two other peaks present – one with binding energy of 286.6 eV (13.6-18.9 %), corresponding to C–O, as well as a peak with a binding energy of 288.9 eV (13.9%), corresponding to the double bonds C=O. The O1s spectra contain two components corresponding to the different iron oxides (FeO and Fe_3O_4), with binding energies of 530 and 530.9 eV, respectively, and two components attributed to single (49.3%) and double (35.8%) C–H energies of 532.1 and 533.6 eV, respectively. These lines can be safely attributed to EG moieties remaining on the surface of MNPs in accordance with the findings from FTIR measurements.

Table 2. Elemental composition of the MNPs and MNPs-Bpy samples obtained by XPS and XRF data.

Sample	Elements concentration							
	at %(XPS)				at %(XRF)		wt %(XRF)	
	Fe	O	C	Sm	Fe	Sm	Fe	Sm
Sm:MNPs	18.2 ± 1.5	38.2 ± 1.1	35.5 ± 1.0	8.1 ± 0.5	97.44	2.27	93.8 ± 0.6	5.9 ± 0.01
Sm:MNPs-Bpy	13.7 ± 1.4	33.4 ± 0.8	43.1 ± 1.1	9.9 ± 0.5	95.14	2.83	90.6 ± 0.6	7.3 ± 0.01

Coming back to the definition of the valence state of Fe in our samples, one can look for the presence or absence of certain characteristic features in the spectrum of iron. This feature is a component C, which is present in Fe2p spectrum of Sm:MNPs (see. Fig.5b) and absent in the iron spectrum of Sm:MNPs-Bpy. This feature is located 8.2 eV higher than Fe2p$_{3/2}$ peak, and its presence is characterized by XPS Fe2p spectrum of Fe(III) [30]. This component is the so-called "shake-up" satellite or charge transfer satellite [30-32]. In the case of Fe2p spectrum of Fe_3O_4 sample the charge transfer satellite is absent [32]. Thus, the proximity of Fe2p$_{3/2}$ energy position to the table value for magnetite and especially difference in charge transfer satellite can attribute the sample to magnetite mainly. Each of Fe2p$_{3/2}$ spectra in Fig. 5 has a shoulder A' at a low-energy side, which also requires an interpretation. By interpreting it worth to take into account that magnetite has a spinel structure, where tetrahedral sites are occupied by Fe^{2+}ions, and those octahedral – by Fe^{3+} ions. At low temperatures, the ratio between Fe^{2+}: Fe^{3+} should be 1:2 [32]. In [34] the same shoulder in Ni2p$_{3/2}$ spectrum was explained by the presence of divalent and trivalent nickel ions in $Ni_{1-x}Co_xCr_2O_4$ spinel structure, and the shoulder formed by the contribution from divalent nickel ions. If this approach is applicable to magnetite in respect to the explanation of the shoulder in Fe2p$_{3/2}$ spectrum, the contribution of Fe^{2+} ions into total Fe2p spectrum is higher in Sm:MNPs-Bpy than in Sm:MNPs. Assuming that in Fe2p spectrum of Fe(II) the satellite is located much closer to the main peak (~ 5 eV), the presence of Fe^{2+} ions in enough large quantity in Sm:MNPs-Bpy should lead to a broadening of Fe2p$_{3/2}$ spectrum of the sample and to the absence of charge transfer satellite in the region of 18.5 eV in Fig. 5b, as in our case. In this regard, the reduction of A' shoulder in Fe2p$_{3/2}$ spectrum of Sm:MNPs and appearance of C satellite may indicate that there are more Fe^{3+} ions in the sample in respect to Sm:MNPs-Bpy, which does not allow to define this sample as pure magnetite. This finding permits us to attribute the crystal phase of Sm:MNPs to maghemite (γ-Fe_2O_3) as having the same spinel ferrite structure as magnetite. Hence, both materials are expected to be ferrimagnetic.

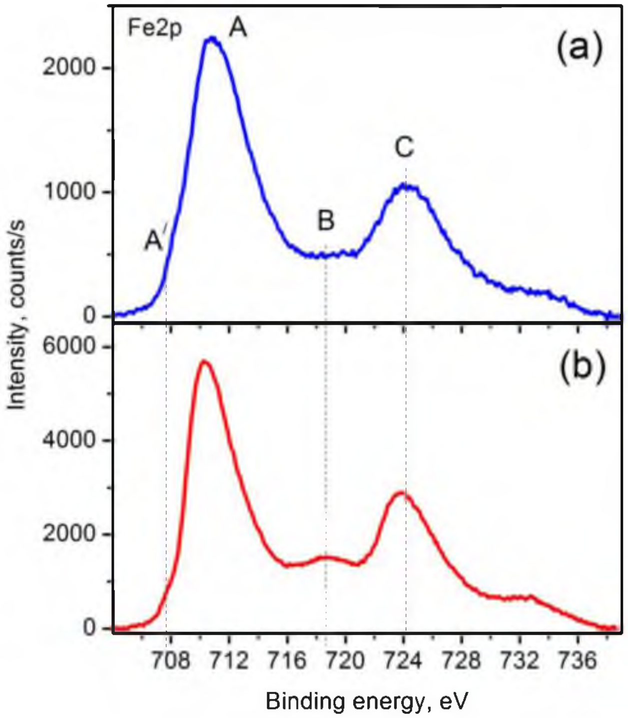

Fig. 5. XPS Fe2p spectra of Sm:MNPs-Bpy (a) and Sm:MNPs (b) samples.

The magnetization field dependences demonstrate hysteresis, which cannot be explained by a simple super paramagnetic behavior. The model designed by M. Chuev and J. Hesse [35] was used. It extends the well-known Stoner-Wohlfarth model describing the magnetic properties of single-domain MNPs in combination with the Neel's ideas concerning the dynamical behavior and magnetization relaxation in such systems. The coercivity observed for Sm:MNPs exceeds one for the sample Sm:MNPs-Bpy in 8 times (see the insert in the Fig.6). This corresponds the two times difference in particles dimensions in spite of the rather wide size dispersion. The saturation magnetization is comparable in the samples under study. The values of saturation magnetization Ms, remanent magnetization Mr, coercivity Hc, and squareness Sr (Sr~Mr/Ms) of MNPs are presented in Table 3.

Table 3. Magnetic properties of the MNPs and MNPs-Bpy samples.

Sample	H_c (Oe)	M_s (emu/g)	M_r (emu/g)	Sr
Sm:MNPs	88.8	71.6	12	0.17
Sm:MNPs-Bpy	13.3	68.8	3.3	0.05

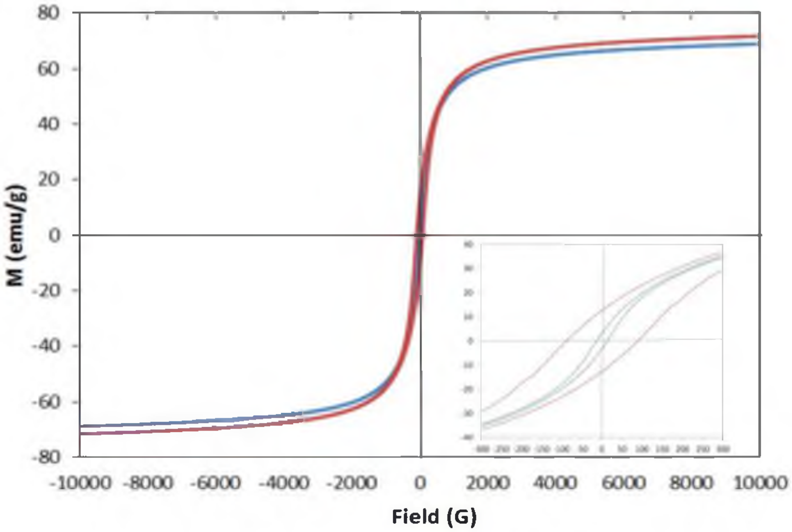

Fig.6. M-G loops for Sm:MNPs (red) and Sm:MNPs-Bpy (blue) samples measured at RT; inset zooms hysteresis at low fields.

The presumed mechanism of MNPs formation can be described according to [36-37]:

$$CH_2OH - CH_2OH \rightarrow CH_3CHO + H_2O \qquad (1.1)$$

$$2Fe^{3+} + 2\,CH_3CHO + OH^- \rightarrow 2Fe^{2+} + CH_3CO - COCH_3 + 2H_2O \qquad (1.2)$$

The reduction is based on the decomposition of EG and its conversion to butanedione [38]. At the first stage (dehydration of EG) an intermediate product, acetaldehyde, can be produced [39]. Fe^{3+} ions from initial salt and Fe^{2+} ions prepared by reduction with acetaldehyde may produce magnetite MNPs by co-precipitation [40]:

$$Fe^{2+} + 2Fe^{3+} + 8OH^- \rightarrow Fe_3O_4 + 4H_2O \qquad (1.3)$$

From (1.3) it can be seen that alkaline media is necessary for the reduction Fe^{3+} to Fe^{2+}. During synthesis EG reacts as both reduction agent and solvent.

Experimental data gave no evidence of residual presence of Bpy molecules: in XPS profile there is no signal from a nitrogen atom at 403.3 eV (N1s) seen in [16], and no IR vibrations like C=N (1492 cm^{-1}) and C_2–N (1323 cm^{-1}) observed in [41]. There is no distinct signs for the presence of Bpy in TGA profile, whose desorption could be expected at about 190 and 290 °C [41]. This might be rationalized by the following: it is known that 2,2'-Bpy posses a weak coordination effect to the NPs surface, while providing a major steric stabilization effect [16]. Due to steric hindrance of 2,2'-Bpy molecule it would not cover entire MNPs, but might align along the chains of octahedral Fe ions from the outermost layer of Fe_3O_4 (001) surface [17]. Due to expected mismatch in distances and shielding from neighboring oxygen a strong bidentate interaction, which would safe this molecules from being washed out from the surface with any given solvent is unfavorable.

4. Conclusions

By efficient solvothermal polyol synthesis we obtained the iron oxide MNPs characterized by narrow distribution and hydrophilic surface. Taking into account their magnetic properties, they can be classified as SPIONs ready for biomedical applications. Introduction of 2,2'-Bpy during the synthesis allows to reduce the average MNPs size more than twice, and preserve magnetite phase against partial oxidation into maghemite. There is no traces of 2,2'-Bpy left on samples, but its role during nucleation and growth of particles apparently is not limited to simple stabilization and worth of a specific study. And as far as magnetic properties of prepared MNPs are concerned, more detailed study at various temperatures and different magnetic field rates is planned and the theoretical model of M. Chuev and J. Hesse [35] should be modified taking into account the MNPs size dispersion.

Acknowledgments

The TEM, XRD and TG data were obtained at the joint research center "Diagnostics of structure and properties of nanomaterials" of Belgorod National Research University. This work was supported by the Russian Science Foundation (grant № 14-35-00051).

References

1. S.P. Gubin. Magnetic Nanoparticles. John Wiley & Sons, Weinheim, 2009, 484 pages.
2. X.J. Loh, T-C. Lee, Q. Dou and G.R. Deen, Utilising inorganic nanocarriers for gene delivery, Biomater. Sci. 4 (2016) 70–86.
3. Z. Li, E. Ye, David, R. Lakshminarayanan, X.J. Loh, Recent Advances of Using Hybrid Nanocarriers in Remotely Controlled Therapeutic Delivery, Small 12 (2016) 4782–4806.
4. C. Sun, J.S.H. Lee, M. Zhang. Magnetic nanoparticles in MR imaging and drug delivery, Adv. Drug. Deliv. Rev. 60 (2008) 1252–1265.
5. S.-H. Huang, R.-S. Juang. Biochemical and biomedical applications of multifunctional magnetic nanoparticles: a review, J. Nanopart. Res. 13 (2011) 4411–4430.
6. K. Huang, Q. Dou, X.J. Loh, Nanomaterial mediated optogenetics: opportunities and challenges, RSC Adv. 6 (2016) 60896–60906.

7. G.J. Strijkers, W.J.M. Mulder, G.A.F. van Tilborg, K. Nicolay, MRI Contrast Agents: Current Status and Future Perspectives, Anticancer Agents Med. Chem. 7 (2007) 291–305.
8. T.A. Lastovina, A.L. Bugaev, S.P. Kubrin, E.A. Kudryavtsev, A.V. Soldatov, Structural studies of magnetic nanoparticles doped with rare-earth elements, J. Struct. Chem. 57 (2016) 1444–1449;
9. B.M. Teo, D.J. Young, X.J. Loh, Magnetic Anisotropic Particles: Toward Remotely Actuated Applications. Part. Part. Syst. Charact., 33 (2016) 709–728.
10. E. Ye, X.J. Loh, Polymeric Hydrogels and Nanoparticles: A Merging and Emerging Field, Aust. J. Chem. 66 (2013) 997–1007.
11. T.D. Schladt, K. Schneider, H.Schild, W. Tremel, Synthesis and bio-functionalization of magnetic nanoparticles for medical diagnosis and treatment, Dalton Trans. 40 (2011) 6315–6343.
12. C. Dhand, N. Dwivedi, X.J. Loh, A.N.J. Ying, N.K. Verma, R.W. Beuerman, R. Lakshminarayanan, S. Ramakrishna, Methods and strategies for the synthesis of diverse nanoparticles and their applications: a comprehensive overview, RSC Adv. 5 (2015) 105003–105037.
13. S. Laurent, D. Forge, M. Port, A. Roch, C. Robic, L. Vander Elst, R.N. Muller. Magnetic Iron Oxide Nanoparticles: Synthesis, Stabilization, Vectorization, Physicochemical Characterizations, and Biological Applications, Chem. Rev. 108 (2008) 2064–2110.
14. Z. Stojanović, M. Otoničar, J. Lee, M.M. Stevanović, M.P. Hwang, K.H. Lee, J. Choi, D. Uskoković, The solvothermal synthesis of magnetic iron oxide nanocrystals and the preparation of hybrid poly (L-lactide)–polyethyleneimine magnetic particles, Colloids Surf. B Biointerfaces 109 (2013) 236–243.
15. F. Ooi, J.S. DuChene, J. Qiu, J.O. Graham, M.H. Engelhard, G. Cao, Z. Gai, W.D. Wei, A Facile Solvothermal Synthesis of Octahedral Fe_3O_4 Nanoparticles, Small 11 (2015) 2649–2653.
16. B. Leger, A. Denicourt-Nowicki, H. Olivier-Bourbigou, A. Roucoux, Rhodium Nanocatalysts Stabilized by Various Bipyridine Ligands in Nonaqueous Ionic Liquids: Influence of the Bipyridine Coordination Modes in Arene Catalytic Hydrogenation, Inorg. Chem. 47 (2008) 9090–9096.
17. R. Bliem, J. Pavelec, O. Gamba, E. McDermott, Z. Wang, S. Gerhold, M. Wagner, J. Osiecki, K. Schulte, M. Schmid, P. Blaha, U. Diebold, G.S. Parkinson. Adsorption and incorporation of transition metals at the magnetite Fe_3O_4 (001) surface, Phys. Rev. B 92 (2015) 075440.

18. W. Huan, C. Cheng, Y. Yang, H. Yuan, Y. Li, A Study on the Magnetic and Photoluminescence Properties of Eu^{n+} and Sm^{3+} Doped Fe_3O_4 Nanoparticles, J. Nanosci. Nanotechnol. 12 (2012) 4621–4634.
19. C.R. De Silva, S. Smith, I. Shim, J. Pyun, T. Gutu, J. Jiao, Z. Zheng. Lanthanide(III)-Doped Magnetite Nanoparticles, J. Am. Chem. Soc. 131 (2009) 6336–6337.
20. X-ray diffraction by polycrystalline materials. By R. Guinebretiere. Pp. 351. London: ISTE, 2007.
21. ICDD PDF data card numbers (a) 01-089-0691, (b) 01-085-1436, (c) 01-089-0688.
22. M. Al-Haj, Structural characterization and magnetization of $Mg_{0.7}Zn_{0.3}Sm_xFe_{2-x}O_4$ ferrites. J. Magn. Magn. Mater. 299 (2006) 435–439.
23. L. Guo, X. Shen, X. Meng, Y. Feng, Effect of Sm^{3+} ions doping on structure and magnetic properties of nanocrystalline $NiFe_2O_4$ fibers, J. Alloys Compd. 490 (2010) 301–306.
24. Z.L. Wang, Transmission Electron Microscopy of Shape-Controlled Nanocrystals and Their Assemblies, J. Phys. Chem. B 104 (2000) 1153–1175.
25. T.R. Bastami, M.H. Entezari, High stable suspension of magnetite nanoparticles in ethanol by using sono-synthesized nanomagnetite in polyol medium. Mater. Res. Bull. 48 (2013) 3149–3156.
26. C.B. Sekaran, P.L. Tirupatamma, V. Rajitha, K. Vishnupriya, B. Jayasree, Assay of ezetimibe in bulk and in its pharmaceutical formulations by spectrophotometry, Int. J. Pharm. Pharm. Sci, 4 (2012) 396–401.
27. A. Schlegel, S.F. Alvarado, P. Wachter, Optical properties of magnetite (Fe_3O_4), J. Phys. C: Solid State Phys. 12 (1979) 1157–1164.
28. J.K. Vassiliou, V. Mehrotra, M.W. Russell, E.P. Giannelis, R.D. McMichael, R.D. Shull, R.F. Ziolo, Magnetic and optical properties of γ-Fe2O3 nanocrystals. J. Appl. Phys. 73 (1993) 5109–5116.
29. G.B. Deacon and R.J. Ppillips, Relationships between the carbon-oxygen stretching frequencies of carboxylato complexes and the type of carboxylate coordination, Coord. Chem. Rev. 33 (1980) 227–250.
30. D. Briggs, John T. Grant Surface Analysis by Auger and X-Ray Photoelectron Spectroscopy, IM Publications (2003) 840 pp.
31. A.T. Kozakov, A.G. Kochur, K.A. Googlev, A.V. Nikolsky, I.P. Raevski, V.G. Smotrakov, V.V. Eremkin X-ray Photoelectron study of the valence state of iron in iron – containing single – crystal ($BiFeO_3$, $PbFe_{1/2}Nb_{1/2}O_3$), and ceramic ($BaFe_{1/2}Nb_{1/2}O_3$) multi ferroics, J. Electron Spectrosc. Relat. Phenom. 184 (2011) 16–23.

32. T. Yamashita, P. Hayes. Analysis of XPS spectra of Fe^{2+} and Fe^{3+} ions in oxide materials. Appl. Surf. Sci. 254 (2008) 2441–2449.
33. V. I. Nefedov, X-Ray Photoelectron Spectroscopy of Chemical Compounds. Handbook [in Russian], Nauka, Moscow (1984) 256 pp.
34. A.G. Kochur, A.T. Kozakov, K.A. Googlev, A.S. Mikheykin, V.I. Torgashev, A.A. Bush, A.V. Nikolskii, Chemical bonding and valence state of 3d-metal ions in $Ni_{1-x}Co_xCr_2O_4$ spinels from X-ray diffraction and X-ray photoelectron spectroscopy data. J. Electron. Spectrosc. 195 (2014) 208–219.
35. M.A. Chuev and J. Hesse, Nanomagnetism: extension of the Stoner–Wohlfarth model within Néel's ideas and useful plots, J. Phys. Condens. Matter 19 (2007) 506201.
36. L. Bai, J. Fan , Y. Cao, F. Yuan, A. Zuo, Q. Tang, Shape-controlled synthesis of Ni particles via polyol reduction, J. Cryst. Growth. 311 (2009) 2474–2479.
37. M. Tsuji, M. Kubokawa, R. Yano, N. Miyamae, T. Tsuji, M.-S. Jun, S. Hong, S. Lim, S.-H. Yoon, I. Mochida, Fast Preparation of PtRu Catalysts Supported on Carbon Nanofibers by the Microwave-Polyol Method and Their Application to Fuel Cells, Langmuir, 23 (2007) 387–390.
38. C.N.R. Rao, A. Müller, A.K. Cheetham, The Chemistry of Nanomaterials: Synthesis, Properties and Applications, John Wiley & Sons, 2006, 761 pp.
39. T. Sugimoto, Monodispersed Particles, Elsevier, 2001. 820 pp.
40. M. Su, C. He, K. Shih, Facile synthesis of morphology and size-controlled α-Fe_2O_3 and Fe_3O_4 nano-and microstructures by hydrothermal/solvothermal process: The roles of reaction medium and urea dose, Ceram. Int. 42 (2016) 14793–14804.
41. D.C. Onwudiwe, C.A. Strydom, The bipyridine adducts of N-phenyldithiocarbamato complexes of Zn(II) and Cd(II); synthesis, spectral, thermal decomposition studies and use as precursors for ZnS and CdS nanoparticles, Spectrochim. Acta A 135 (2015) 1080–1089.

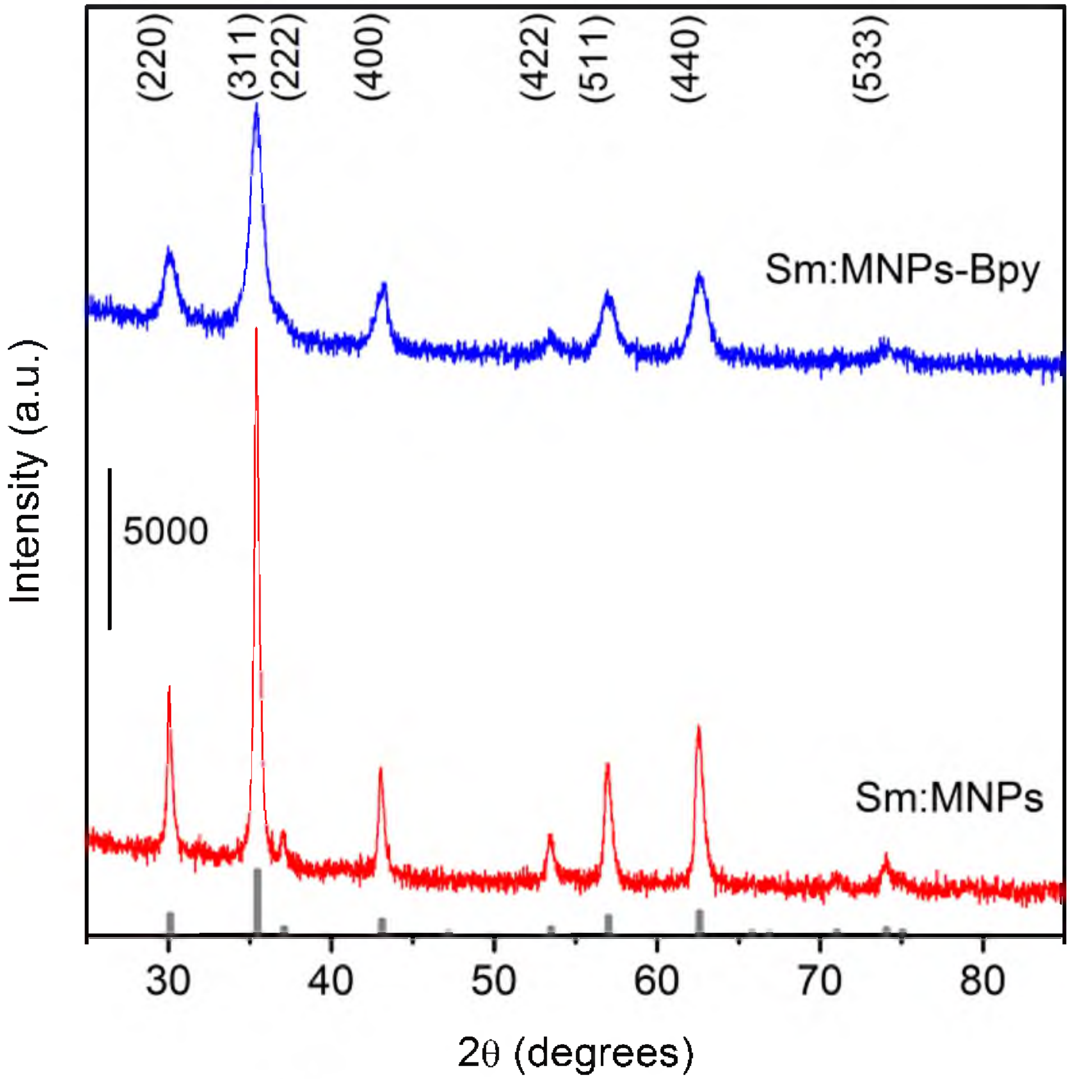
(220)
(311)
(222)
(400)
(422)
(511)
(440)
(533)
Sm:MNPs-Bpy
Intensity (a.u.)
5000
Sm:MNPs
30
40
50
60
70
80
2θ (degrees)

Fig. 1

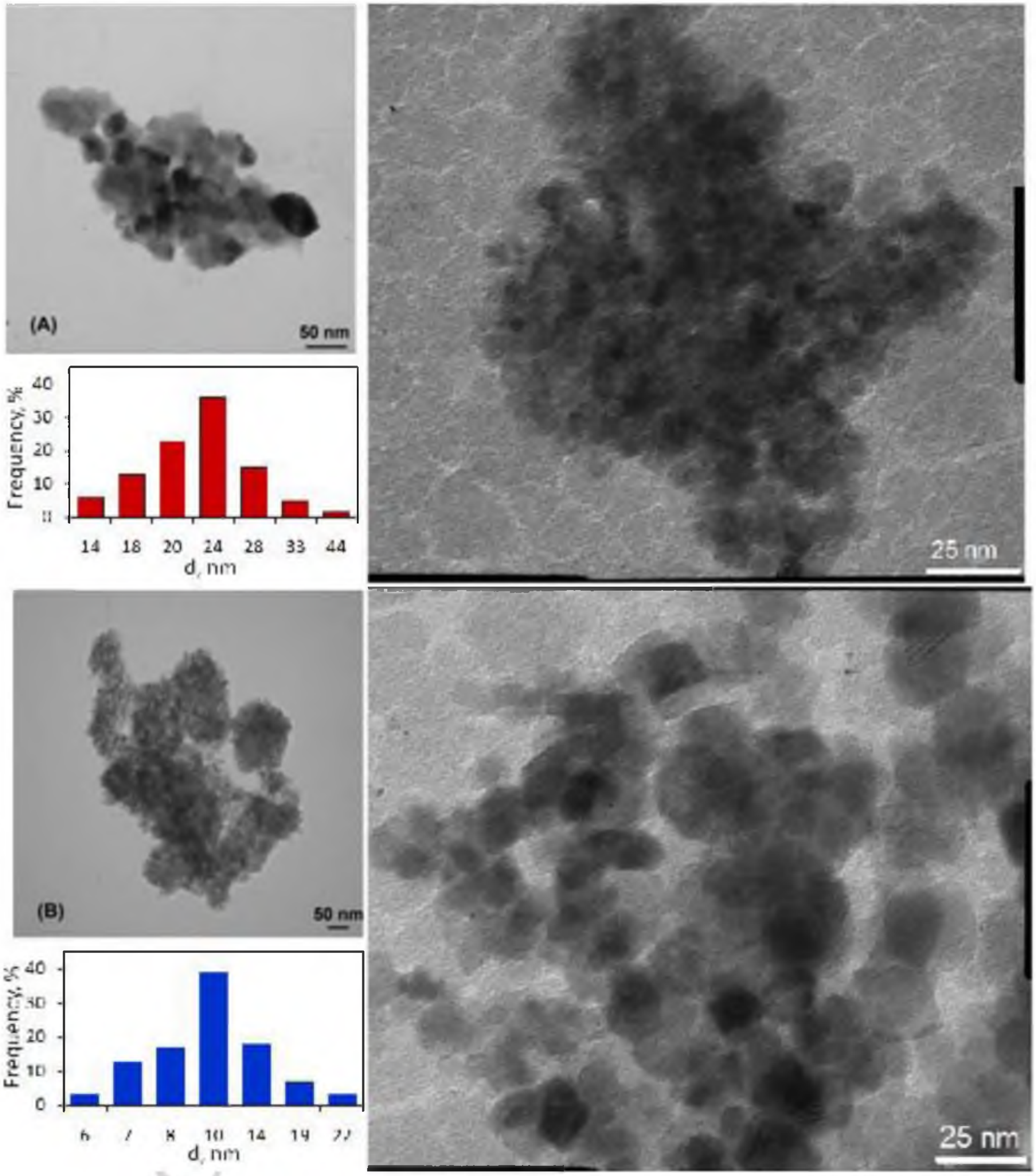
(A)
50 nm
Frequency, %
0
10
20
30
40
14
18
20
24
28
33
44
d, nm
25 nm
(B)
50 nm
Frequency, %
0
10
20
30
40
6
7
8
10
14
19
22
d, nm
25 nm

Fig. 2

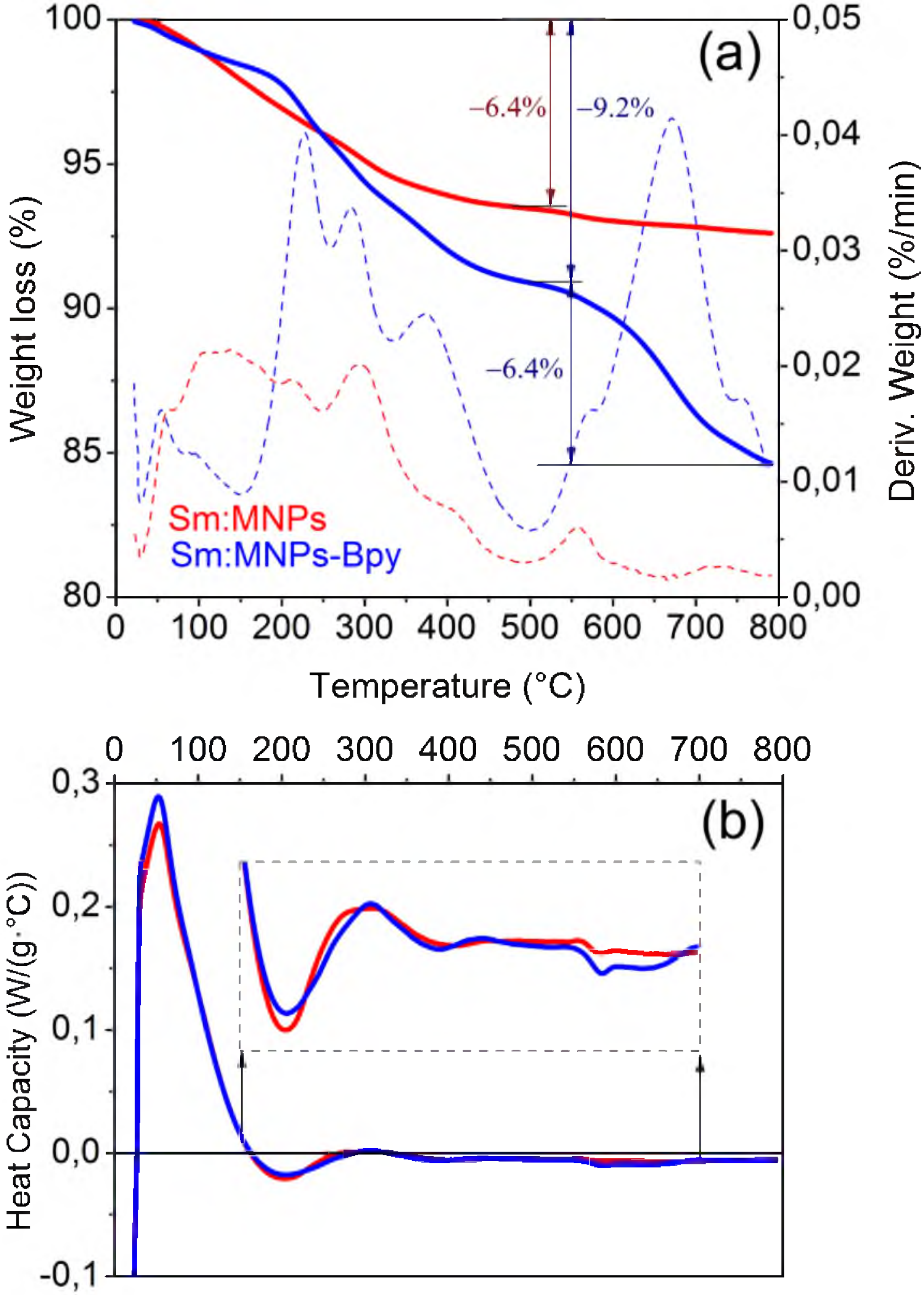
(a)
Weight loss (%)
100
95
90
85
80
Deriv. Weight (%/min)
0,05
0,04
0,03
0,02
0,01
0,00
–6.4%
–9.2%
–6.4%
Sm:MNPs
Sm:MNPs-Bpy
0
100
200
300
400
500
600
700
800
Temperature (°C)
(b)
0
100
200
300
400
500
600
700
800
Heat Capacity (W/(g·°C))
0,3
0,2
0,1
0,0
-0,1

Fig. 3

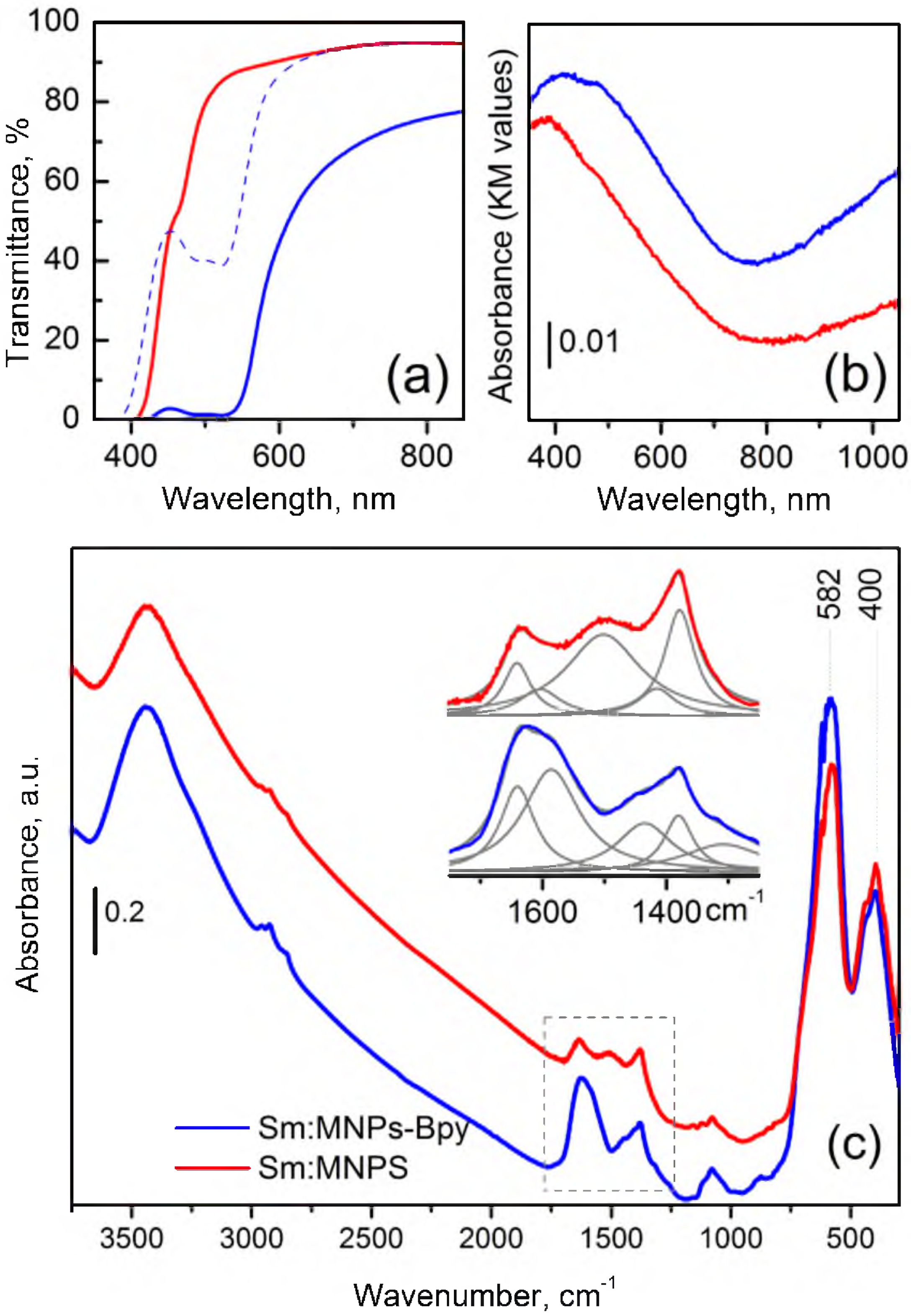
100
80
60
40
20
0
Transmittance, %
400
600
800
Wavelength, nm
(a)
Absorbance (KM values)
0.01
400
600
800
1000
Wavelength, nm
(b)
582
400
1600
1400
cm^{-1}
Absorbance, a.u.
0.2
Sm:MNPs-Bpy
Sm:MNPS
(c)
3500
3000
2500
2000
1500
1000
500
Wavenumber, cm^{-1}

Fig. 4

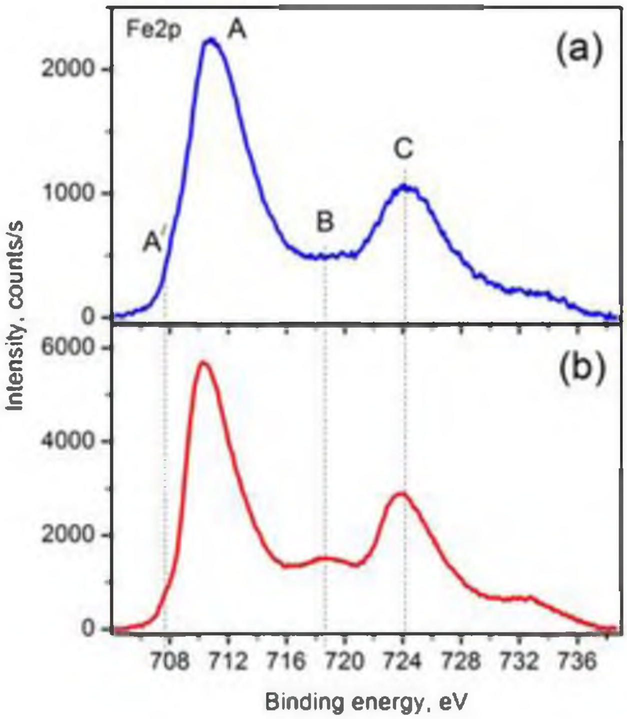
Fe2p
A
A′
B
C
(a)
(b)
2000
1000
0
6000
4000
2000
0
Intensity, counts/s
708
712
716
720
724
728
732
736
Binding energy, eV

Fig. 5

Table 1. XRD and TEM analysis data for Sm:MNPs and Sm:MNPs-Bpy samples

Sample name	Phase name	Space group	Lattice parameter, **a** (A)	Crystallite size, **d'** (nm)	Crystallite size, **d"** (nm)	Particle size, **d*** (nm)
Sm:MNPs	Magnetite, syn	Fd-3m	8.3972	24.5 ±2.30	24.7607	23.8
Sm:MNPs-Bpy	Magnetite	Fd-3m	8.3936	8.9 ±0.83	6.9134	9.6

Note: crystallite size **d'** is calculated by Sherrer's relation, and **d" -** by Williamson-Hall method. Particle size **d*** d from the analysis of TEM images.

Table 2. Elemental composition of the MNPs-Bpy and MNPs samples obtained by XPS and XRF data.

Sample	Elements concentration							
	at %(XPS)				at %(XRF)		wt %(XRF)	
	Fe	0	C	Sm	Fe	Sm	Fe	Sm
Sm:MNPs	18.2 ± 1.5	38.2 ± 1.1	35.5 ±1.0	8.1 ±0.5	97.44	2.27	93.8 ± 0.6	5.9 ±0.01
Sm:MNPs-Bpy	13.7 ±1.4	33.4 ±0.8	43.1 ±1.1	9.9 ±0,5	95.14	2.83	90.6 ± 0.6	7.3 ± 0,01

Highlights:

- Sm^{3+}-doped magnetite nanoparticles were obtained by solvothermal polyol method,
- Magnetic nanoparticles are twice smaller if 2,2'-bipyridine is used as a capping agent,
- Sm^{3+}-doped magnetite nanoparticles have clean surface and are useful as a MRI contrast agent.